

pubs.acs.org/cm Article

Lyotropic Liquid Crystalline Mesophase Governs Interfacial Molecular Orientation of Conjugated Polymer Thin Films

Ge Qu, Kyung Sun Park, Prapti Kafle, Fengjiao Zhang, Justin J. Kwok, Bijal B. Patel, Detlef-M. Smilgies, Lars Thomsen, Christopher R. McNeill, and Ying Diao*



Cite This: Chem. Mater. 2020, 32, 6043-6054



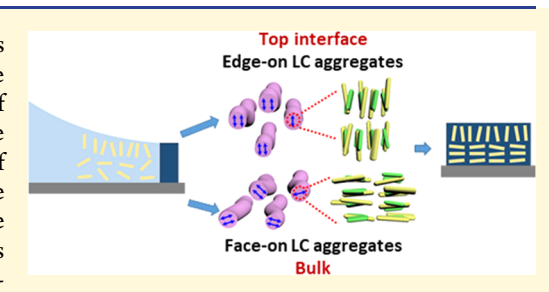
ACCESS

III Metrics & More

Article Recommendations

SI Supporting Information

ABSTRACT: Interfacial out-of-plane molecular orientation critically influences the electronic performance of organic semiconductor thin films. The appearance of a lyotropic liquid crystalline (LC) mesophase during solution coating of conjugated polymers may directly determine the interfacial out-of-plane molecular orientation. However, a lack of studies on the packing structure of the liquid crystalline mesophase and its evolution to the solid state impedes the general understanding of the molecular orientation transformation from the liquid crystalline mesophase to solid-state thin films. This work addresses this unanswered question using poly[[2,5-bis(2-octadecyl)-2,3,5,6-tetrahydro-3,6-diketopyrrolo[3,4-c]pyrrole-1,4-diyl]-alt-(2-octylnonyl)-2,1,3-benzotriazole]



(DPP-BTz) as a model compound. From near-edge X-ray adsorption fine structure spectroscopy and grazing incidence wide-angle X-ray scattering (GIWAXS) measurements, we observe distinct edge-on orientation at the top interface compared to a primarily face-on orientation in the bulk in solution-coated DPP-BTz thin films. Interestingly, the interfacial orientations in thin films are strongly correlated with those of the lyotropic liquid crystalline mesophase of DPP-BTz appearing during solution coating. Specifically, the LC mesophase adopts an edge-on orientation near the air—liquid interface and a face-on orientation in the bulk liquid layer. The multiscale structure and interfacial orientation of the mesophase are characterized by solution-state small-angle X-ray scattering and in situ GIWAXS measurements. We attribute the edge-on LC orientation at the top interface to surface energy minimization of alkyl side chains with air, while the anisotropic broad LC orientation distribution in the bulk arises from twisted molecular packing in the LC mesophase. The out-of-plane molecular orientation is preserved in the LC mesophase and is carried over to the solid-state thin film, creating the distinct edge-on interfacial alignment at the thin-film top surface.

■ INTRODUCTION

Solution-processable conjugated polymers have been intensively studied as candidates for next-generation electronics owing to their rich chemical diversity and superior properties for fabricating lightweight, flexible, and high-performing electronic devices. As a fabrication method adaptable to industrial-scale manufacturing processes, meniscus-guided coating enables deposition of conjugated polymers with abundant tunable coating conditions. Much effort has been dedicated to designing conjugated polymers and optimizing solution coating methods to attain desirable thin-film morphologies and charge transport properties. 1,2 Out-ofplane molecular orientation serves as a critical factor determining organic electronic device properties, through modulating the ionization potential of organic semiconductor (OSC) thin films and electronic coupling at the OSC heterojunctions.³⁻⁵ Mixed "face-on" and "edge-on" molecular orientations in conjugated polymer thin films may also contribute to high charge carrier mobilities through the creation of three-dimensional charge transport pathways. 6,7 Many methods have been adopted to tune the out-of-plane molecular orientation of organic semiconductors, which can be

categorized into two groups: tuning molecular interaction and applying an external field. Tuning molecular interactions includes tuning molecular self-interaction, molecule—solvent interaction, and/or molecule—substrate interaction by molecular design, solution choice, substrate modification, substrate modification, substrate also been used to tune molecular orientation and alignment. While most of these studies have focused on characterizing or tuning molecular orientation, few have investigated how the assembly process resulted in the observed molecular orientation in the first place. Further, understanding how interfacial orientation differs from the ensemble average across the film thickness is imperative but understudied. Such lack of fundamental understanding severely impedes our ability

Received: April 1, 2020 Revised: June 23, 2020 Published: June 24, 2020





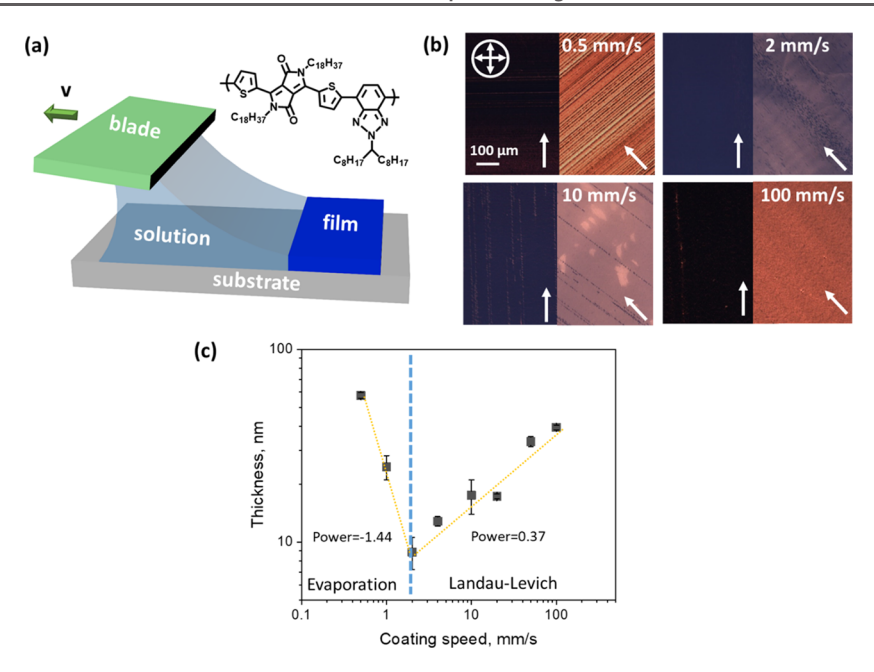


Figure 1. Solution coating of DPP-BTz thin films and speed series on SiO₂ substrates. (a) Schematic of meniscus-guided coating of DPP-BTz conjugated polymers. (b) Cross-polarized microscopy images of DPP-BTz thin films coated on SiO₂ substrates at 0.5, 2, 10, and 100 mm/s coating speeds. The arrows indicate the coating direction. The cross refers to the orientation of the polarizer and the analyzer of the microscope. (c) Correlation between coated film thickness and coating speed. The black squares are experimental data, and the dotted lines are from data fitting to determine the thickness—coating speed relationship in the evaporation and Landau—Levich regimes.

to control molecular orientation and interfacial properties by rational design.

Here, we focus on drawing a link between solution-state assembly and the resulting solid-state molecular orientation and interfacial morphology. We are particularly interested in how the presence of a lyotropic liquid crystal mesophase in solution mediates molecular orientation and alignment in thin films. Thermotropic liquid crystalline conjugated polymers have been investigated in the past few decades for which thermal annealing is commonly used to induce LC phase transformation for enhancing charge transport properties. 17-19 Lyotropic conjugated polymers have come to the attention of the field only recently despite their direct relevance to solution processing. Conjugated polymer systems that are reported to show lyotropic liquid crystalline behavior include PCDTPT/ PCDTBT, 20-22 P(NDI2OD-T₂), 23 P3ATs, 24-27 and DTFPbased polymers^{28,29} However, most of the donor-acceptor conjugated polymers do not have reported lyotropic LC phases. 20,21 Specifically of relevance to this work, there is rarely (if any) a report on the lyotropic LC behavior of diketopyrrolopyrrole (DPP)-based donor-acceptor polymers. In our recent work, we observed lyotropic LC mesophases in two widely studied donor-acceptor conjugated polymer systems—poly[3,3'-bis(4-decyl-1-tetradecyl)-6,6'-bis(thienyl-5-yl)-isoindigo] (PII-2T) and poly[[2,5-bis(2-octadecyl)-2,3,5,6-tetrahydro-3,6-diketopyrrolo[3,4-c]pyrrole-1,4-diyl]-alt-(2-octylnonyl)-2,1,3-benzotriazole] (DPP-BTz).30 We found that the relative torsional backbones of PII-2T and DPP-BTz are conducive to form chiral twist-bent nematic phases; planarization of the polymer backbone by printing flow eliminates the twist-bent mesophase to result in drastically enhanced alignment in printed films.³⁰ Aside from our work, in-plane alignment of lyotropic conjugated polymers has been previously studied by multiple groups. 21,23,28 With regard to out-of-plane molecular orientation, Trefz, Ludwigs, and

colleagues found that solution-coated lyotropic $P(NDI2OD-T_2)$ exhibits a distinct edge-on orientation at the film surface, whereas the bulk film can be either face-on or edge-on depending on the blade coating temperature. Despite these thorough studies, the evolution of LC phase molecular orientation and its relationship with thin-film interfacial molecular orientation has yet to be discussed. Additionally, for the few studies on lyotropic LCs, the structure of the LC phase has been rarely reported, which impedes the understanding of how the LC structure carries over to the film.

In this work, we study a high-performance donor-acceptor conjugated polymer DPP-BTz and observe a distinct interfacial molecular orientation in solution-coated thin films directed by the structure of a liquid crystalline mesophase. Controlling crystallinity and in-plane alignment of DPP-BTz using innovative solution coating techniques has been recently reported.31,32 This work particularly focuses on understanding the out-of-plane molecular orientation of DPP-BTz in relationship to the structure of its lyotropic liquid crystalline phase, which has not been previously studied. Characterized by grazing incidence wide-angle X-ray scattering (GIWAXS) and near-edge X-ray adsorption fine structure (NEXAFS) spectroscopy, DPP-BTz molecules show edge-on orientation at the top interface while assuming a preferential face-on orientation in the bulk film. We discovered a lyotropic liquid crystalline mesophase of DPP-BTz appearing at the meniscus front during solution coating and characterized its molecular and mesoscale structure using small-angle X-ray scattering (SAXS) and in situ GIWAXS measurements during solution coating. Based on our proposed liquid crystalline structure, we elucidate that DPP-BTz liquid crystals have a preferred face-on orientation in the bulk of the liquid layer and a predominantly edge-on orientation at the top air-liquid interface in the meniscus. Upon further solvent evaporation, the liquid crystalline mesophase transfers its structural characteristics into dried

polymer films, preserving the out-of-plane molecular orientation distribution. Studying the lyotropic liquid crystalline behavior of conjugated polymers provides new opportunities in understanding the complex conjugated polymer assembly during processing, which in turn enables modulating the structure and properties of conjugated polymers at the molecular level.

■ RESULTS

In this study, we adopted meniscus-guided coating (MGC)^{30,33,34} to deposit DPP-BTz thin films at different speeds onto various substrates from 10 mg/mL chlorobenzene solution at an elevated substrate temperature of 80 °C (Figure 1a). A series of substrates were tested with surface energies ranging from 20.5 to 52.2 mN/m to establish the generality of LC-guided interfacial orientations. The substrate surface chemistries tested include OTS, PVDF-HFP, PTS, PVP:HDA, and bare SiO₂ (see the SI experimental section for full names). We will first discuss results on SiO₂ substrates followed by comparison across all substrates. On SiO2 substrates, we varied coating speeds from 0.5 to 100 mm/s to cover both the evaporation regime and the Landau-Levich regime.³⁵ The optical microscopy images of the thus-coated DPP-BTz thin films are shown in Figure 1b, with the coating direction oriented 0 and 45° with respect to either the polarizer or the analyzer to observe birefringence and to infer alignment of crystalline domains. The birefringence between the 0° and the 45° image indicated moderate in-plane alignment within the coated film. The extent of interfacial in-plane alignment is further quantified by NEXAFS measurements and will be discussed later. The atomic force microscopy (AFM) measurements at the cross section of the films show decreased and then increased film thickness, indicating crossing of coating regimes with increasing coating speed (Figure 1c).35 The low-speed evaporation regime is governed by mass transport from evaporation-driven capillary flow, where the film thickness decreases with the increasing coating speed. The high-speed Landau-Levich regime is dominated by viscous-force-driven convective flow, where film thickness increases with coating speed. In this case, the transition coating speed is 2 mm/s with the lowest film thickness at 8.9 nm. Both the evaporation regime and the Landau-Levich regime exhibit power-law dependence of the film thickness with coating speed. The power-law exponents in the evaporation regime and the Landau-Levich regimes are -1.44 and 0.37, respectively, both deviating from the corresponding theoretical values of -1 and 0.67.35 The difference between experiment and theory may result from the nonideal conditions during solution coating, such as partial wetting and stick-slip instability,³⁶ Marangoni flow, 35 skin-layer formation, 33 and dependence of assembly pathways (and therefore viscosity) on coating regimes.³⁰

We performed a partial pole figure analysis from the GIWAXS 2D scattering patterns to quantitatively analyze the out-of-plane molecular orientation of DPP-BTz polymers in the thin film. Measurements of the top interface and the bulk film are differentiated by varying the incident angle of the X-ray beam, 0.04° for interfacial measurements and 0.14° for bulk measurements. The 0.14° incident angle is slightly above the critical angle for total reflection at the polymer—air interface, yielding a penetration depth of the complete film thickness, while the shallow 0.04° incident angle gives a penetration depth of 5–8 nm, approximately 3–4 molecular layers. The GIWAXS 2D patterns for the top interface and

the bulk film coated at 0.5 mm/s are shown in Figure 2a,b. The (100) lamellar stacking peak is analyzed to construct the partial

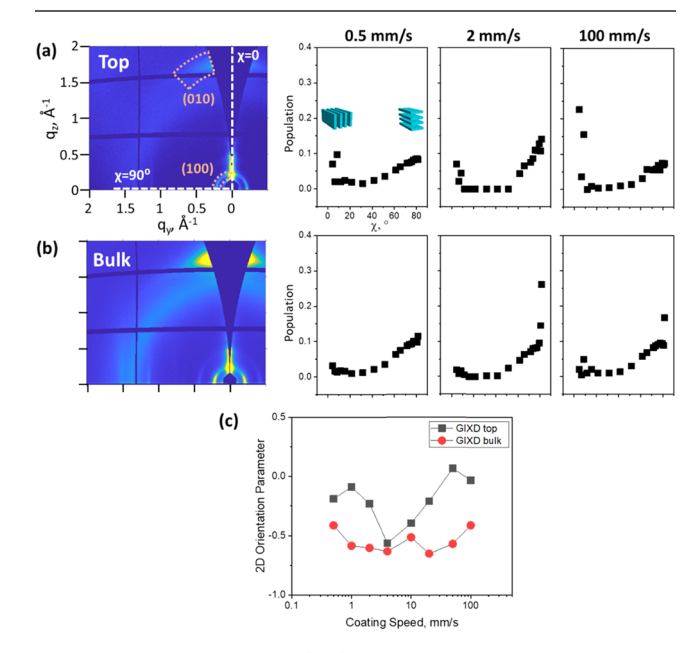


Figure 2. Two-dimensional (2D) grazing incidence X-ray scattering patterns for films coated at 0.5 mm/s and partial pole figure results for films coated at 0.5, 2, and 100 mm/s for the (a) top interface and (b) bulk film. Measurements are taken with the incident beam perpendicular to the coating direction. (c) Out-of-plane 2D orientation parameter from GIWAXS measurements at various coating speeds.

pole figures and quantify the out-of-plane polymer orientation in the crystalline domains. The (100) peak is chosen because it has high intensity and narrow peak width in the $\chi = 0-90^{\circ}$ range compared to the (010) peak and is less affected by the "missing wedge" after geometric correction, as shown in the GIWAXS patterns in Figure 2a. The partial pole figures are obtained by plotting the (100) lamellar peak intensity from 1° sector cut profiles on the geometrically corrected scattering patterns within the range of $4 < \chi < 82^{\circ}$. We note that a narrow sector cut is essential for capturing the sharp change of intensity near the pole and horizon (Figure 2a). For the (100) lamellar stacking peak, the intensity near $\chi = 0^{\circ}$ corresponds to edge-on crystallites and the intensity near $\chi = 90^{\circ}$ corresponds to face-on crystallites. The peak intensities are normalized to the 0-1 scale for direct comparison of the polymer orientations across different coating speeds and interfaces/

As shown in Figure 2, the pole figures at 0.5, 2, and 100 mm/s represent the thin-film out-of-plane orientation in the evaporation, transition, and Landau–Levich regimes, respectively (complete set of pole figures in Figure S1). At the top interface, a sharp rise of intensity near $\chi=0^\circ$ reveals the presence of edge-on crystallites, with the highest population observed at the highest coating speeds of 50–100 mm/s. However, in the bulk film, a sharp increase in intensity is observed near $\chi=90^\circ$ corresponding to face-on crystallites. The highest intensity at $\chi=90^\circ$ for the bulk film appears at a coating speed of 4 mm/s, in the neighborhood of the transition regime. Overall, from the pole figure analysis, we observe distinct edge-on crystallites residing at the top interface of the film, as compared to the predominance of face-on crystallites in

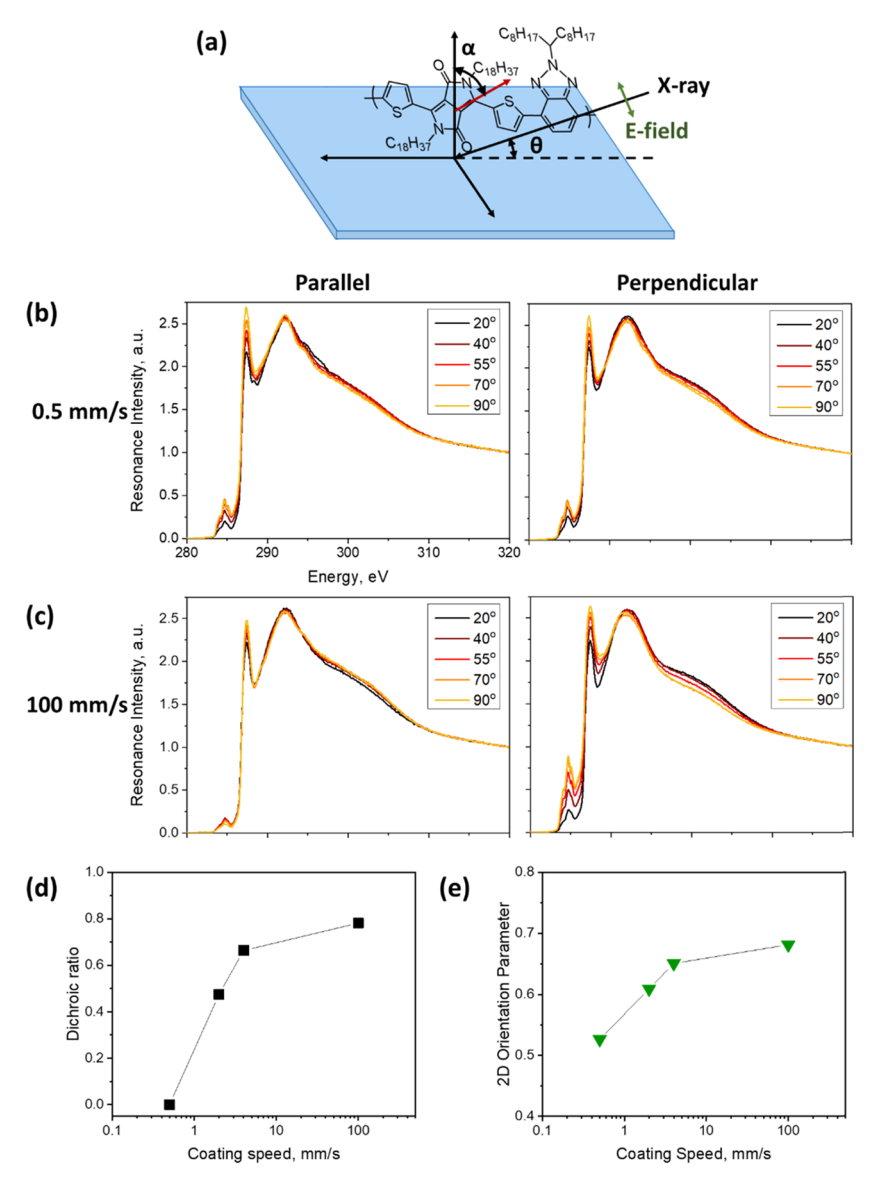


Figure 3. Angle-resolved NEXAFS measurement illustration and results. (a) Illustration of NEXAFS measurements of the DPP-BTz polymer with the incident angle θ using a polarized X-ray beam. The angle between the transition dipole moment of the DPP-BTz molecule with respect to the substrate normal is α . Angle-resolved NEXAFS spectra with the X-ray beam parallel and perpendicular to the coating direction at (b) 0.5 mm/s and (c) 100 mm/s are shown. Calculated (d) dichroic ratio of in-plane alignment and (e) out-of-plane 2D orientation parameter from NEXAFS measurements at various coating speeds.

the bulk of the film. The degree of out-of-plane orientation from GIWAXS measurements is quantified in terms of the 2D orientation parameter $S_{\rm 2D} = 2\langle \cos^2 \gamma \rangle - 1$, where γ is the tilt angle of the conjugated backbone with respect to the substrate (Figure 2c). 31,39,40 Within a scale of $S_{\rm 2D}$ between -1 and 1, S=1 indicates a completely edge-on orientation, S = 0 indicates an isotropic orientation, and S = -1 indicates a completely faceon orientation. Detailed calculation of $S_{\rm 2D}$ is included in the Supporting Information. S_{2D} from GIWAXS of top interfaces and the bulk film reside in the range from -0.6 to 0, corresponding to a preferred face-on orientation, with a moderate coating speed dependence. The $S_{\rm 2D}$ of the top interface is closer to zero (less face-on) compared to $S_{\rm 2D}$ of the bulk, due to the emergence of edge-on crystallites at the top interface. The S_{2D} values for the top interface and the bulk film meet at 4 mm/s in the neighborhood of the transition regime, where the film is as thin as 12.8 ± 0.7 nm, possessing a relatively homogeneous out-of-plane molecular orientation.

The GIXD measurements with the incident angle below the critical angle are not truly surface sensitive, as the X-ray penetration depth is still 5-8 nm. This is reflected by $S_{\rm 2D}$ values close to those of bulk films. We employed NEXAFS spectroscopy to obtain the out-of-plane molecular orientation of the topmost molecular layer. Incident-angle-resolved NEXAFS measurements with a polarized X-ray beam are used to probe the K-shell electron C 1s $-\pi^*$ resonance and collect angle-dependent absorption spectra. Because the transition dipole moment of the C $1s-\pi^*$ resonance is orthogonal to the conjugated plane, the orientation of the conjugated polymer backbone is determined by analyzing the C 1s- π^* intensity obtained from multiple tilt angle θ scans (Figure 3a). Unlike GIWAXS, NEXAFS measurements do not distinguish crystalline or amorphous regions but instead give an averaged molecular orientation information with contribution by all polymers.

Tilt-angle NEXAFS scans are performed at incident angles 20, 40, 55, 70, and 90°, with the incident X-ray beam both parallel and perpendicular to the coating direction. NEXAFS measurements are operated under the partial electron yield mode, probing the top 3 nm of the thin film (~1 molecular layer). Figure 3b,c shows example spectra of tilt-angle measurements on films coated at 0.5 and 100 mm/s with the X-ray beam both parallel and perpendicular to the coating direction. The complete set of NEXAFS spectra from 0.5, 2, 4, and 100 mm/s films is included in Figure S2. For quantitative analysis, the intensity of the C 1s $-\pi^*$ resonance peak at 285 keV is analyzed. At 0.5 mm/s, the angle-resolved NEXAFS scans are similar in parallel and perpendicular measurements, with increasing intensity from 20 to 90° . On the other hand, at 2, 4, and 100 mm/s, the angle-resolved spectra from parallel scans nearly overlay across the range of angles scanned, but spectra from perpendicular scans show significant angle dependence. The difference between parallel and perpendicular scans arises because the intensity variation of the C 1s $-\pi^*$ resonance depends on the relative alignment between the polarized X-ray beam and the transition dipole moment (TDM) of the molecule. In an aligned film, the maximum degree of TDM variation occurs in the direction orthogonal to the polymer backbone, where TDM is parallel to the substrate for the edge-on backbone and normal to the substrate for the face-on case. Therefore, a minimum angle-dependent signal in parallel measurements and a significantly angle-dependent signal in perpendicular measurements indicate a preferred inplane polymer backbone alignment along the coating direction. The dichroic ratio calculated by $DR_{\text{NEXAFS}} = \frac{I_{90^{\circ},\text{perp}} - I_{90^{\circ},\text{par}}}{I_{90^{\circ},\text{perp}} + I_{90^{\circ},\text{par}}}$ increased from 0 to 0.78 for films coated at 0.5-100 mm/s (Figure 3d). This indicates an increasing degree of in-plane alignment with increasing coating speed at the top interface.

We further extracted out-of-plane molecular orientation from the angle-resolved NEXAFS spectra in perpendicular measurements. The strongest resonance signal occurred when the linearly polarized X-ray beam aligned with the TDM of the C 1s $-\pi^*$ resonance. We observed the strongest C 1s $-\pi^*$ intensity at $\theta = 90^{\circ}$, which indicated a predominant TDM orientation parallel to the substrate, or equivalently a primarily edge-on orientation of the polymer at the very top molecular layer. Across all experimental conditions tested, we observed increasing C 1s $-\pi^*$ intensity with increasing incident angle θ (Figure S2), indicating that DPP-BTz at the film surface adopts a preferential edge-on orientation. We further evaluated the 2D orientation parameter S_{2D} to quantitatively express the molecular orientation in the topmost layer. Due to the biaxial alignment of DPP-BTz in thin films, calculation of $S_{\rm 2D}$ requires angle-resolved NEXAFS spectra from both parallel and perpendicular measurements. 41 Fitting parameters are obtained from the intensity of the C 1s $-\pi^*$ resonance and the average out-of-plane orientation $\langle \cos^2 \alpha \rangle$ in terms of the TDM tilt angle α with respect to the substrate normal (details in the Experimental Section). We obtained S_{2D} values in the range of 0.53-0.68 (Figure 3e), confirming a preferential edge-on orientation. S_{2D} only slightly increases when varying the coating speed from 0.5 to 100 mm/s, showing a very weak speed dependence. We believe that the molecular orientation in the topmost layer is dictated by interfacial properties, not by processing conditions, as discussed later.

The combined out-of-plane 2D orientation parameter S_{2D} from both GIWAXS and NEXAFS measurements are shown in

Figure 4a (tabulated in Table S1). It is clear that S_{2D} values from GIWAXS measurements (-0.65 to 0.07) for the top

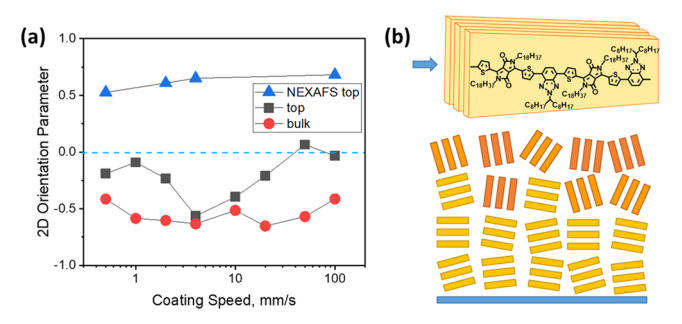


Figure 4. Out-of-plane 2D orientation parameter and the corresponding morphology. (a) Combined plot for the 2D orientation parameter $S_{\rm 2D}$ calculated from GIWAXS and NEXAFS measurements. (b) Illustration of the out-of-plane molecular orientation of DPP-BTz thin films from various coating speeds. The rectangles represent a side view of DPP-BTz crystallites viewed down the polymer backbone.

interface and bulk film indicate preferential face-on orientation of crystallites, while $S_{\rm 2D}$ values from NEXAFS measurements (0.53–0.68) at the very top interface suggest favorable edge-on orientation of the backbone. The large discrepancy between the top-surface $S_{\rm 2D}$ values from GIWAXS (–0.56 to 0.07) and NEXAFS (0.53–0.68) is likely due to different penetration depths of the X-ray beam (5–8 vs ~3 nm). In other words, near-surface GIWAXS measurements have significant contributions from the bulk film. Inferring from the above $S_{\rm 2D}$ analysis, we illustrate the out-of-plane molecular orientation distribution shown in Figure 4b: the polymers adopt an edge-on orientation at the very top interface of the thin film, while the bulk films consist of face-on crystallites, agreeing with literature findings. 23,37,42

Additionally, we fabricated field-effect transistor devices to measure the hole mobility at the top and the bottom interface. We constructed top gate bottom contact (TGBC) devices for top interface measurements and bottom gate top contact (BGTC) devices for bottom interface measurements (Figure 5a,b). The field-effect mobility $\mu_{\rm sat}$ is calculated from the transfer curves in the saturation regime. Devices with their channel length parallel and perpendicular to the coating direction are fabricated to evaluate the charge transport anisotropy, which is defined by $\mu_{\rm par}$ over $\mu_{\rm perp}$. The characteristic transfer and output curves comparing TGBC and BGTC devices and the extracted top and bottom interface mobilities are shown in Figure 5a,b. The majority of the charge transport mobility at the top interface is higher than that at the bottom interface. The highest hole mobility at the top interface (TGBC) reaches 0.57 cm²/(V·s), compared to 0.011 cm²/(V· s) for the bottom interface (BGTC) (Figure 5c,d). However, because different dielectrics are used for the top interface (440 nm polymethyl methacrylate) and the bottom interface (300 nm SiO₂) device fabrication, mobility values from the two interfaces are not directly comparable.

While the absolute mobility values are not comparable, charge transport anisotropy can be compared between top and bottom interfaces. The charge transport anisotropy is calculated as $A = \mu_{\rm par}/\mu_{\rm perp}$ and is shown in Figure 5e. The top interface exhibits significantly higher hole mobilities in the parallel direction, yielding a high charge transport anisotropy compared to the bottom interface. The highest mobility

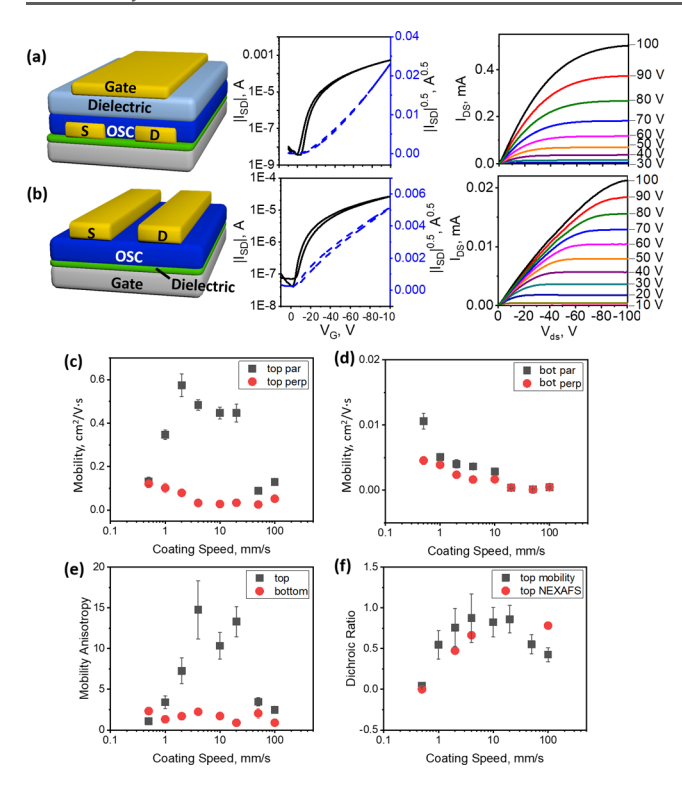


Figure 5. Field-effect transistor device configuration, saturation regime transfer curves, and output curves for (a) top interface and (b) bottom interface charge transport characteristic measurements. Charge carrier mobilities at the (c) top interface and (d) bottom interface with the transport direction parallel and perpendicular to the coating direction. (e) In-plane charge carrier mobility anisotropy calculated by the ratio of parallel versus perpendicular mobility at the top and the bottom interface. (f) Comparison of the mobility dichroic ratio with the in-plane alignment from NEXAFS measurements at the top interface.

anisotropy of A = 14.7 at the top interface occurs at 4 mm/s, which is consistent with the highly aligned polymer backbone at the top interface. The bottom interface shows very low or almost no charge transport anisotropy, with the highest anisotropy A = 2.3 at 0.5 mm/s. The dichroic ratio of charge transport is calculated from the anisotropy as $DR_{transport} = \frac{A-1}{A+1}$ to compare with the dichroic ratio of polymer backbone alignment from NEXAFS. For charge transport, DR = 1 indicates charge transport only along the coating direction and DR = -1 indicates a charge transport completely orthogonal to the coating direction. As shown in Figure 5f, the trend of the charge transport dichroic ratio closely follows that from NEXAFS. Both dichroic ratios are close to zero at 0.5 mm/s and increase with speed at 2 and 4 mm/s, which suggests faster charge transport along the polymer backbone at the top interface, agreeing with our previous work.³³ The increasing backbone alignment with coating speed from NEXAFS is attributed to the increase of the extensional strain rate at the top interface of the meniscus.³⁰ At 100 mm/s, while the top surface is still highly aligned as indicated by NEXAFS, the contribution of polymer morphology to mobility is likely more than 1 molecular layer, leading to the discrepancy between mobility and the alignment dichroic

After determining the solid-state out-of-plane molecular orientation of DPP-BTz thin films, we probed the solution-

state structure using cross-polarized microscopy and in situ microbeam GIWAXS to understand the evolution of the DPP-BTz assembly process when the film is drying to correlate the solution-state structure with the film morphology. We first recorded the top-view meniscus movement under crosspolarized microscopy. Interestingly, we observed the appearance of a birefringent blue band at the front of the meniscus (Figure 6a). The birefringent blue band traces the movement of the meniscus as shown in Supporting Video 1, which belongs to the highest concentration region of the meniscus. This is because the solution concentration increases rapidly from the bulk to the triple-phase contact line due to solvent evaporation,³⁰ reaching the critical concentration for the appearance of the lyotropic liquid crystalline mesophase. We note that optical birefringence was used to infer the liquid crystalline (LC) mesophase for conjugated polymers in previous reports. 23,30 To determine the presence of the LC mesophase and its concentration range, DPP-BTz solution in chlorobenzene at a high concentration was made and inspected under a cross-polarized microscope (Figure 6b). We found that vibrant birefringence under cross-polarizers in the entire solution attributed to the bulk LC mesophase was visible at 100 mg/mL, as compared to no LC texture from 10 and 60 mg/mL. One signature of the LC mesophase is its birefringence when rotating the sample (Supporting Video 2). Therefore, we deduce that DPP-BTz undergoes isotropicto-mesophase transition during solution coating when chlorobenzene continuously evaporates and the polymer concentration approaches 100 mg/mL. The structure and the orientation of the LC mesophase may influence the final out-of-plane orientation of the conjugated polymer in the thinfilm state, which we discuss in detail below.

We determine the molecular-scale structure of LC and its orientation distribution during solution coating to correlate with thin-film morphology by performing in situ microbeam grazing incidence wide-angle X-ray scattering (µGIWAXS) measurements during solution coating of DPP-BTz on SiO2 substrates with the incident X-ray beam perpendicular to the coating direction. The data from perpendicular measurements is representative of the entire film at the specific coating condition studied (0.5 mm/s); Figure S3 shows that similar out-of-plane molecular orientation distributions are obtained from both parallel and perpendicular measurements in thin films coated at this condition. In μ GIWAXS, the X-ray beam is focused with an X-ray focusing capillary into a width of 40 μ m, yielding high spatial resolution during in situ X-ray measurements without compromising the signal-to-noise ratio. 43 In the scattering video, a broad transient halo centered at q = 1.45Å⁻¹ first emerges from the horizon and forms a complete ring. Subsequently, this halo disappears as the π - π stacking peak and the lamellar stacking peaks emerge (Supporting Video 3). Figure 6c comprises time-lapsed snapshots of the scattering video showing the background, the rise of the transient halo, the complete transient halo, and the appearance of stacking peaks when the halo disappears. To better visualize and analyze the in situ μ GIWAXS data, an intensity-time-q plot is constructed for coating of the DPP-BTz solution at 0.5 mm/s, highlighting evolution of important peaks including the transient halo, the (100) lamellar stacking peak, the (010) π - π stacking peak, and the amorphous peak (Figure 6d). The broad transient halo (q of 1-2 Å^{-1}) appears around 3 s and disappears at 4 s after the coating blade passed the beam, followed by the rise of the (100) peak ($q = 0.22 \text{ Å}^{-1}$), the

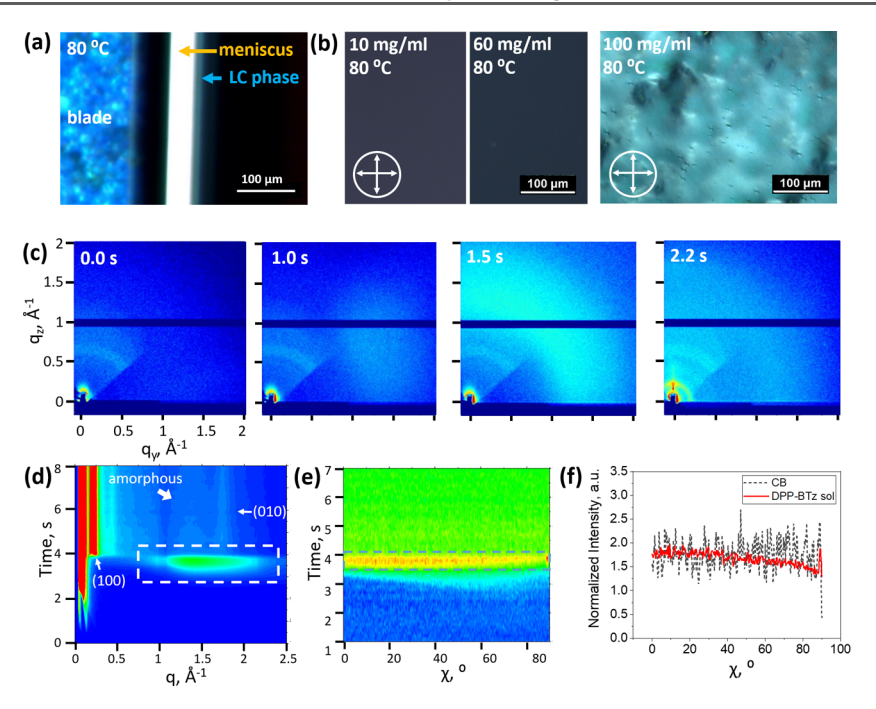


Figure 6. Microscopy and in situ GIWAXS measurements of liquid crystalline DPP-BTz. (a) In situ cross-polarized microscopy of the meniscus during solution coating of 10 mg/mL DPP-BTz in chlorobenzene solution on SiO₂ substrates at 80 °C with 1 mm/s coating speed. (b) Cross-polarized microscopy images of the bulk liquid crystalline mesophase of DPP-BTz in chlorobenzene with 10, 60, and 100 mg/mL concentrations at 80 °C. (c) Evolution of scattering peaks from in situ μGIWAXS measurements during solution coating of 5 mg/mL DPP-BTz at 0.5 mm/s at 70 °C on SiO₂ substrates. The same conditions apply to (d-f). (d) Intensity—time—q plot with $\chi = 0-90^{\circ}$. This plot shows the evolution of peaks with respect to time across the range of q values. Peak locations are determined from this plot. (e) Normalized intensity—time— χ plot for q = 0.8-0.95 Å⁻¹. This plot shows the χ angle-dependent intensity distribution of the transient halo centered at 1.45 Å⁻¹ evolving with time. The q range is selected to be q = 0.8-0.95 Å⁻¹ instead of near 1.45 Å⁻¹ to avoid the effect of gap in the detector on scattering intensity. The y-axis time scales in (d) and (e) are the same for direct comparison. (f) Dependence of the transient halo scattering intensity on the χ angle comparing the cases of the neat chlorobenzene solvent (black dashed line) and the 5 mg/mL DPP-BTz solution (red solid line).

(010) peak ($q = 1.75 \text{ Å}^{-1}$), and the amorphous peak (q = 1.44 \mathring{A}^{-1}) after 4 s. A transient halo also appears when coating pure chlorobenzene solvent on the substrate (Supporting Video 4). However, the scattering intensity is 30 times weaker than the case of coating DPP-BTz chlorobenzene solution. Because an LC mesophase is observed at the meniscus front during solution coating (Figure 6a), the scattering intensity is expected to have contributions from the LC mesophase in this q range. We anticipate that the average $\pi - \pi$ spacing in the LC phase is close to that in the amorphous phase due to rotational disorder, which we have shown in our previous work.30 To validate this point, we make the normalized intensity—time— γ plot to determine the intensity distribution of the transient peak over the γ angle (Figure 6e). Such a plot can help differentiate the anisotropic scattering of the LC mesophase (χ angle dependent) from the isotropic scattering of the solution (χ angle independent). The polar angle χ on the scattering pattern is defined as $\gamma = 0$ for the vertical and $\gamma =$ 90° for the horizontal direction. In the intensity—time— χ plot for coating of the DPP-BTz solution, the intensity of the transient peak at its maximum has an anisotropic distribution across $\chi = 0-90^{\circ}$. The intensity is high in the $\chi = 0-50^{\circ}$ range and decreases in the range $\chi = 50-85^{\circ}$, and then, a sharp peak appears near $\chi = 90^{\circ}$. This indicates that the species contributing to the transient halo scattering has preferential out-of-plane orientation distribution in contrast to the pure solution with isotropic scattering intensity (Figure S4a). A more direct comparison by plotting the line-cut at the maximum intensity from the intensity—time— χ plot is shown

in Figure 6f for pure solvent vs. DPP-BTz solution. The chlorobenzene data is noisy because of the low intensity of pure solvent scattering but still shows homogeneous distribution over χ . Meanwhile, the DPP-BTz solution coating intensity distinctly decreases in the range $\chi = 50-85^{\circ}$, leaving an overall high intensity in the range $\chi = 0-50^{\circ}$ and a sharply peaked intensity at $\chi = 90^{\circ}$. We believe that solvent and solvated polymer aggregates contribute to isotropic intensity distribution in the transient peak, but the LC mesophase with a preferred out-of-plane orientation gives rise to the anisotropic intensity distribution. The origin of the χ angle-dependent intensity with a higher intensity in the low χ range and the sharp intensity peak near $\chi = 90^{\circ}$ will be analyzed in the Discussion section.

We further characterized the mesoscale structure of the LC mesophase using solution SAXS (Figure S5). We observed a broad peak centered at 0.191 Å $^{-1}$ in the background-subtracted SAXS 1D profile for both 10 and 100 mg/mL DPP-BTz solutions (Figure S5a). We attributed this structure factor to loose lamellar stacking with a d-spacing of 32.9 Å compared to a lamella stacking of 28.7 Å in solid thin films (Figure S5b-d; detailed discussion in the Supplementary Note). Further, the rising intensity at the low q region indicates the presence of preaggregates for both 10 and 100 mg/mL solutions (Figure S5a). Thus, we infer that the loose lamella stacking occurs inside the preaggregates.

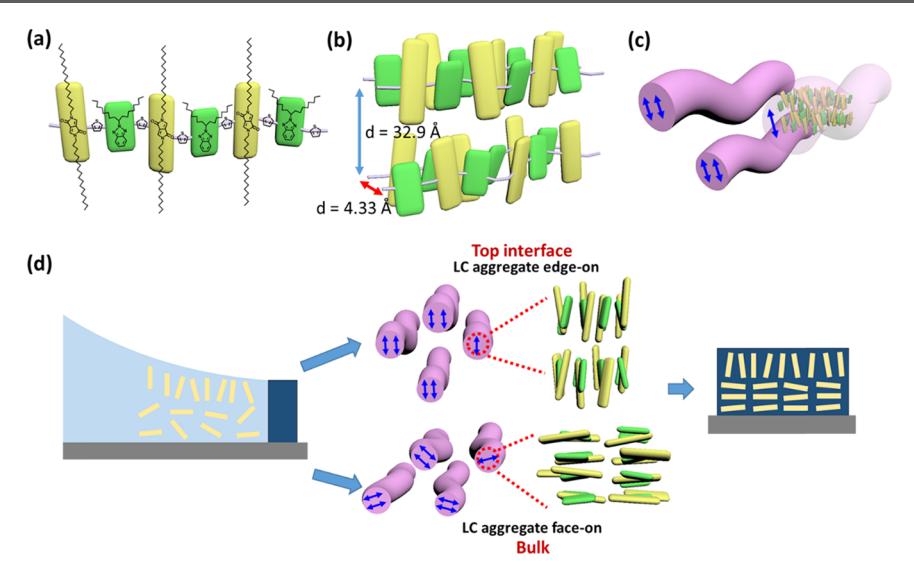


Figure 7. Schematic of the liquid crystal structure and the link between solution- and solid-state interfacial orientations. (a) DPP-BTz polymer backbone with DPP (yellow bars) and BTz (green bars) units. (b) Illustration of molecular-scale structural features within the aggregate that constitutes the liquid crystal mesophase, with average polymer backbone spacing of 4.33 Å and lamella layer distance of 32.9 Å. (c) Twist—bend aggregates forming the LC mesophase. The polymer backbone is along the aggregate long axis. The blue arrow in the cross section of the aggregate indicates the direction of lamellar stacking. (d) DPP-BTz assembly through the liquid crystalline mesophase with distinct out-of-plane orientation at the top vs in the bulk film. The yellow rectangles represent the side view of the polymer backbone.

DISCUSSION

Based on the thin-film NEXAFS data, in situ μ GIWAXS data, and solution-state SAXS data, we propose the DPP-BTz liquid crystalline structure and the mechanism by which the LC mesophase determines the interfacial orientation in the solid thin film. Figure 7a-c summarizes the molecular and mesoscale structural features of the LC mesophase. We infer from SAXS results (Figure S5) that the LC mesophase comprises preaggregates rather than dispersed single polymer chains. As the solution concentration increases during solvent drying, the volume density of polymer aggregates crosses a critical threshold to form a "colloidal" liquid crystal phase. The aggregates exhibit both loose π - π and lamella stacking internally. The average $\pi - \pi$ spacing is obtained from the q value of the transient halo at $q = 1.45 \text{ Å}^{-1}$, which gives an average d-spacing of 4.33 Å (Figure 6c). This value is comparable to the average $\pi - \pi$ spacing in the amorphous phase and is substantially larger than the π - π stacking distance of 3.63 Å $(q = 1.73 \text{ Å}^{-1})$ in crystalline domains. The loosely associated π planes in the LC phase eventually evolve into close $\pi - \pi$ stacking when the film solidifies. The average lamella spacing in the LC phase is 32.9 Å, which evolves into a closer lamella stacking at a spacing of 28.7 Å when solidified into a thin film. At the same time, paracrystalline disorder drastically reduces from the LC phase to the solid state, as evidenced by peak sharpening (Figure S5).

The orientation distribution of the LC mesophase can be inferred from the anisotropic intensity distribution of the $\pi-\pi$ stacking ring over χ from in situ μ GIWAXS measurements (Figure 6f). The scattering intensity near $\chi=0$ is contributed by face-on backbones in the LC mesophase. The intensity near $\chi=90^{\circ}$ can be contributed together by the edge-on LC mesophase and the Yoneda peak, a distinct feature of grazing incidence scattering. The majority of LCs in the bulk adopt a moderate face-on orientation, resulting in a higher intensity at $\chi=0-50^{\circ}$. Meanwhile, the LC at the very top interface may

adopt an edge-on orientation. However, its scattering intensity may be buried by the Yoneda peak near $\chi = 90^{\circ}$ in Figure 6f.

After elucidating the LC structure and orientation in the meniscus, we correlate the out-of-plane orientation of the LC mesophase with the orientation in thin films during the process of solution coating and drying (Figure 7d). The lyotropic LC mesophase forms at the front of the meniscus when the critical concentration is reached (between 60 and 100 mg/mL) by solvent evaporation during solution coating of DPP-BTz from chlorobenzene. Because of surface energy minimization, alkyl chains prefer to stick out of the air-liquid interface, leading to edge-on orientation of the mesophase at the top interface. The LC mesophase in the bulk liquid layer may adopt a twisted backbone conformation and a chiral helical assembly found in our previous work.³⁰ The chirality of the mesophase is validated by solution-state cyclic circular dichroism (CD) spectroscopy measurements (Figure S6). The twisted, helical structure may hinder rapid crystallization in the bulk that favors edge-on crystallites. Both the twisted backbone and the slow crystallization kinetics may result in the broad intensity distribution at $\chi = 0-50^{\circ}$ in Figure 6d and a moderate face-on orientation. When the solvent further evaporates, the edge-on LC evolves into edge-on crystallites at the top surface of the dried polymer film, while the face-on LC evolves into face-on crystallites in the bulk of the film. Overall, the crystallization process of DPP-BTz undergoes an isotropic-mesophasesolid-thin-film transition, where the out-of-plane orientation is predetermined by the LC mesophase before evolving into crystallites.

Similar LC-induced out-of-plane orientation distribution in films has been previously reported for discotic small-molecule LCs. Interestingly, many of the conjugated polymers with distinct out-of-plane orientation and in-plane alignment at the top interface versus in the bulk film have a liquid crystalline phase, including P3HT, ^{27,46} DPP-BTz, ^{30,31} P(NDI2OD-T2), ^{23,37} PCDTPT, ^{20,41} etc. There could be a link between distinct interfacial out-of-plane molecular ordering and a liquid-crystal-mediated assembly pathway for conjugated

polymers. The liquid crystalline phase is directional and dynamic and may facilitate rapid molecular reorientation in response to surface properties during the short time scale of printing.

CONCLUSIONS

In summary, we have observed that the formation of the liquid crystalline mesophase governs the out-of-plane molecular orientation distribution in DPP-BTz thin films deposited using meniscus-guided solution coating. As revealed by GIWAXS and NEXAFS measurements, DPP-BTz exhibits an edge-on orientation at the top interface of the film, while adopting a face-on orientation in the bulk film. We discover a lyotropic liquid crystalline mesophase at the meniscus front during solution coating by microscopy and utilize X-ray measurements to elucidate the packing structure of the LC mesophase. Solution SAXS and in situ μ GIWAXS during coating suggest a lamella spacing of 32.9 Å and a π - π spacing of 4.33 Å, respectively. From μ GIWAXS, we also found an anisotropic intensity distribution of the 4.33 Å ring (q = 1.45) $\rm{\AA}^{-1}$) over χ , where high intensity is observed at $\chi = 0-50^{\circ}$ (weakly face-on LC) and a sharp peak appears near $\chi = 90^{\circ}$ (highly edge-on LC). The lamella and $\pi - \pi$ associations in the LC mesophase evolve into lamellar and π - π stacking in the polymer crystallites. Further, the out-of-plane orientation of the LC mesophase directly determines that in the dried film. By revealing a mesophase-mediated assembly pathway and linking the LC phase structure with the thin-film morphology, we enrich our knowledge of conjugated polymer-phase transformation under the evaporative assembly process. Furthermore, our new mechanistic insights can inform strategies to control out-of-plane molecular orientation at interfaces, which is a key parameter modulating the device performance of transistors, solar cells, biosensors, and the effectiveness of molecular doping.

■ EXPERIMENTAL SECTION

Materials. Poly[[2,5-bis(2-octadecyl)-2,3,5,6-tetrahydro-3,6-diketopyrrolo[3,4-c]pyrrole-1,4-diyl]-alt-(2-octylnonyl)-2,1,3-benzotriazole] (DPP-BTz) ($M_{\rm n}=177~{\rm kg\cdot mol}^{-1}$ and PDI = 2.6) was synthesized as reported before. The molecular weight of DPP-BTz was measured by GPC in chlorobenzene at 40 °C. Octadecyltrichlorosilane (OTS, ≥90%), phenyltrichlorosilane (PTS, ≥97%), poly(4-vinylphenol) (PVP, $M_{\rm w}=25~{\rm kg~mol}^{-1}$), and 4,4'-(hexafluoroisopropylidene)diphthalic anhydride (HDA, 99%) were purchased from Sigma-Aldrich. PVDF-HFP with the VDF-to-HFP molar ratio of 55:45 (Dyneon Fluoroelastomer FE) was purchased from 3M Company. All chemicals were used as received.

Conjugated Polymer Thin-Film Preparation. DPP-BTz solution for thin-film printing was prepared by dissolving the conjugated polymer at 10 mg/mL in chlorobenzene and stirred at 40 °C until a homogeneous solution was obtained. DPP-BTz thin films were deposited onto the substrates by a meniscus-guided coating method using an ODTS-treated ${\rm SiO_2}$ blade. The setup included a stationary substrate and a motor-driven blade with the solution sandwiched in between. The blade was set with a tilt angle of 8° and a gap of 100 μ m above the substrate for coating of polymer thin films. The substrate temperature was fixed at 80 °C, and the coating speed was between 0.5 and 100 mm/s.

X-ray Characterizations for Thin-Film and Liquid Crystalline Phase. Static-state grazing incidence wide-angle X-ray scattering (GIWAXS) was performed at beamline 8-ID-E at the Advance Photon Source at the Argonne National Laboratory. Data were collected on a two-dimensional Pilatus 1M detector with an X-ray beam energy at 10.9 keV. Data collection, extraction, and processing

were performed with the GIXSGUI package written for Matlab. Experiments were carried out in a vacuum chamber at room temperature with the incident X-ray angle at 0.14° for bulk film measurements and at 0.04° for surface measurements. Top surface measurements were performed on as-cast films on the substrates. Partial pole figures were constructed by obtaining the intensity of the (100) lamellar stacking peak with respect to the χ angle to study the out-of-plane distribution of the crystallites. The (100) lamellar stacking peak was fitted with a Gaussian function to obtain the peak area and was multiplied with $\sin(\chi)$ at the corresponding χ angle for geometric correction. The pole figures were normalized for cross-sample comparison.

In situ μ GIWAXS was performed at former beamline D1 at the Cornell High Energy Synchrotron Source. Data were collected on a two-dimensional Pilatus 200k detector with an X-ray beam energy at 12.7 keV. The X-ray microbeam was focused by a single-bounce X-ray capillary and was 40 μ m in width to ensure high special resolution during measurement. A meniscus-guided coating setup was installed at the beamline. The blade was tilted at 15°, and the stage temperature was set at 70 °C. The DPP-BTz solution was made in chlorobenzene at the concentration of 5 mg/mL. The solution coating speed was controlled between 0.1 and 0.5 mm/s. The recording rate of the diffraction pattern was up to 50 frames per second, with an exposure time of 0.02 s.

NEXAFS spectroscopy measurements were performed at the Soft X-ray beamline at the Australian Synchrotron. ⁴⁹ Data was acquired using the partial electron yield mode with the photoelectrons emitted from the sample detected using a channeltron detector. Data was analyzed using QANT, ⁵⁰ with further details of analysis methods provided elsewhere. ⁵¹

Two-Dimensional (2D) Orientation Parameter Calculation. We calculated the 2D out-of-plane orientation parameter from both GIWAXS and NEXAFS measurements with the following equation: ^{31,39,40}

$$S_{2D} = \langle \cos 2\gamma \rangle = 2\langle \cos^2 \gamma \rangle - 1$$
 (1)

where γ is the angle between the polymer conjugation plane and the substrate normal. In this case, S=1 indicates a completely edge-on orientation of the molecules, S=0 indicates an isotropic orientation, and S=-1 indicates a completely face-on orientation. We used the 2D orientation parameter because of the ease of evaluating the out-of-plane orientation on the -1 to 1 scale.

For GIWAXS measurements, the averaged out-of-plane orientation of the biaxially aligned crystalline materials is given by 52,53

$$\langle \cos^2 \gamma \rangle_{\text{GIWAXS}} = \frac{\int_0^{\pi} I(\gamma) \cos^2(\gamma) \sin(\gamma) d\gamma}{\int_0^{\pi} I(\gamma) \sin(\gamma) d\gamma}$$
(2)

Partial pole figures were constructed by recording the (100) peak intensity at different χ angles; in this case, the value of χ equals the value of γ . Moreover, because the geometric corrected pole figure intensity is already multiplied with $\sin(\chi)$, the $\sin(\chi)$ in the numerator and the denominator in the above equation is removed. Therefore, $\langle \cos^2 \gamma \rangle$ can be calculated from the results of the pole figures:

$$\langle \cos^2 \gamma \rangle_{\text{GIWAXS}} = \frac{\sum I(\chi)_{i,\text{pole}} \cos^2(\chi)_i \Delta \chi_i}{\sum I(\chi)_{i,\text{pole}} \Delta \chi_i}$$
(3)

where i is the specific data point in the partial pole figures for each condition.

For NEXAFS measurements, the intensity of the C 1s $\to \pi^*$ resonance is dependent on the incident angle θ , assuming a zero-degree molecular pretilt angle:⁴¹

$$I(\theta) = A + B \sin^2(\theta) \tag{4}$$

where A and B are the fitting parameters obtained from measurements with a set of incident angles. Because the DPP-BTz thin films are biaxially aligned, tilt-angle NEXAFS measurements were performed

with the incident beam parallel and perpendicular to the coating direction, giving $A_{\rm para}$, $B_{\rm para}$, $A_{\rm perp}$, and $B_{\rm perp}$ from fitting.

After obtaining the fitted parameters, the theoretical total intensity from NEXAFS can be calculated:

$$I_{\text{tot}} = \frac{3}{2} (A_{\text{para}} + A_{\text{perp}}) + \frac{3P - 1}{2P} (B_{\text{para}} + B_{\text{perp}})$$
 (5)

where P is the polarization factor of the incident X-ray beam and P = 1. The averaged out-of-plane orientation from the NEXAFS can be calculated:

$$\langle \cos^2 \alpha \rangle_{\text{NEXAFS}} = \frac{A_{\text{perp}} + B_{\text{para}} (1 - 1/P)}{I_{\text{tot}}}$$
 (6)

where α is the angle between the π^* TDM and the substrate normal. Because the π^* TDM is orthogonal to the conjugated plane orientation, and γ in eq S1 is defined as the angle between the conjugated plane with the substrate normal, the calculated $S_{\rm 2D}$ from $\langle \cos^2 \alpha \rangle_{\rm NEXAFS}$ need to be multiplied with -1

$$S_{\text{2D, NEXAFS}} = -(2\cos^2\alpha_{\text{NEXAFS}} - 1) \tag{7}$$

The calculated 2D orientation parameters are listed in Table S1.

Field-Effect Transistor Device Fabrication. Top gate bottom contact (TGBC) and bottom gate top contact (BGTC) field-effect transistors were fabricated with DPP-BTz thin films to measure hole mobility at the top and bottom interfaces, respectively. For TGBC devices, 35 nm Ag source/drain electrodes were thermally evaporated onto 300 nm SiO₂ substrates, followed by coating of DPP-BTz thin films. PMMA 80 mg/mL in n-butylacetate solution was prepared and filtered and then spin-coated at 2000 rpm with 500 rpm for 60 s on the DPP-BTz thin films as the dielectric layer. Another layer of 35 nm Ag was evaporated on top of the 450 nm PMMA layer as gate electrodes. BGTC devices were prepared by evaporating 35 nm Ag source/drain electrodes on the DPP-BTz thin film coated on 300 nm SiO₂ substrates. All device measurements were performed with the Keysight B1500A semiconductor parameter analyzer under a nitrogen environment. The field-effect mobilities were calculated in the saturation region of the transfer curves by the equation $I_{\rm DS}=rac{WC_{i^{
m H}}}{2L}(V_{
m G}-V_{
m T})^2$, where $I_{
m DS}$ is the drain-source current; W and L are the conduction channel width and length, respectively; C_i is the capacitance of the dielectric layer (11 nF/cm² for the 300 nm SiO₂ layer and 6.8 nF/cm² for the 450 nm PMMA layer); μ is the apparent mobility; V_G is the gate voltage; and V_T is the threshold voltage.

ASSOCIATED CONTENT

Supporting Information

The Supporting Information is available free of charge at https://pubs.acs.org/doi/10.1021/acs.chemmater.0c01402.

Experimental methods on substrate treatment and solution SAXS measurements; discussion on solution SAXS results and surface energy variation substrate coating series; partial pole figures from GIWAXS for the top interface and bulk for complete coating speed series; NEXAFS PEY tilt-angle spectra; out-of-plane 2D orientation parameter from GIWAXS and NEXAFS; pole figure comparison for incident X-ray parallel and perpendicular to the coating direction; normalized intensity—time— χ plot for the pure solvent and the polymer solution; solution SAXS results and comparison with the solid-state SAXS result; cyclic circular dichroism spectroscopy results; interfacial energy variation substrate coating series results (PDF)

Top view of the solution-coating meniscus front with a liquid crystalline mesophase appearance (MOV)

Bulk liquid crystalline mesophase (MOV)

In situ GIWAXS scattering video for coating of the polymer solution (MOV)

In situ GIWAXS scattering video for coating of the chlorobenzene solvent (MOV)

AUTHOR INFORMATION

Corresponding Author

Ying Diao — Department of Chemical and Biomolecular Engineering, University of Illinois Urbana—Champaign, Urbana, Illinois 61801, United States; orcid.org/0000-0002-8984-0051; Email: yingdiao@illinois.edu

Authors

Ge Qu — Department of Chemical and Biomolecular Engineering, University of Illinois Urbana—Champaign, Urbana, Illinois 61801, United States; © orcid.org/0000-0003-2630-4902

Kyung Sun Park — Department of Chemical and Biomolecular Engineering, University of Illinois Urbana—Champaign, Urbana, Illinois 61801, United States

Prapti Kafle – Department of Chemical and Biomolecular Engineering, University of Illinois Urbana—Champaign, Urbana, Illinois 61801, United States

Fengjiao Zhang — School of Chemical Sciences, University of Chinese Academy of Science, Beijing 100049, China

Justin J. Kwok — Department of Materials Science and Engineering, University of Illinois at Urbana—Champaign, Urbana, Illinois 61801, United States

Bijal B. Patel — Department of Chemical and Biomolecular Engineering, University of Illinois Urbana—Champaign, Urbana, Illinois 61801, United States

Detlef-M. Smilgies — Cornell High Energy Synchrotron Source (CHESS), Ithaca, New York 14853, United States;
ocid.org/0000-0001-9351-581X

Lars Thomsen — Australian Synchrotron, Clayton, Victoria 3168, Australia

Christopher R. McNeill – Department of Materials Science and Engineering, Monash University, Clayton, Victoria 3800, Australia; orcid.org/0000-0001-5221-878X

Complete contact information is available at: https://pubs.acs.org/10.1021/acs.chemmater.0c01402

Notes

The authors declare no competing financial interest.

ACKNOWLEDGMENTS

This research was financially supported by the Office of Naval Research under award #N00014-19-1-2146. Y.D., G.Q., and J.J.K. acknowledge partial support by the National Science Foundation under grant number NSF DMR 18-47828. P.K. acknowledges partial support by the NSF MRSEC: Illinois Materials Research Center under grant number DMR 17-20633. G.Q. acknowledges the Harry G. Drickamer Graduate Research Fellowship. J.J.K. acknowledges the US Department of Energy (DOE) Office of Science Graduate Student Research (SCGSR) Fellowship. The authors acknowledge Seok-Heon Jung and Jin-Kyun Lee from Inha University for synthesizing DPP-BTz used in this research. This research used resources of the Advanced Photon Source, a US Department of Energy (DOE) Office of Science User Facility operated for the DOE Office of Science by Argonne National Laboratory under Contract no. DE-AC02-06CH11357. The authors acknowledge Joseph Strzalka at beamline 8-ID-E and Byeongdu Lee at

beamline 12-ID-B at Advanced Photon Source for help with data acquisition. CHESS was supported by NSF & NIH/NIGMS via NSF award DMR-1332208 at the time of data acquisition. This work was in part performed at the Soft X-ray Beamline of the Australian Synchrotron, part of ANSTO.

REFERENCES

- (1) Diao, Y.; Shaw, L.; Bao, Z.; Mannsfeld, S. C. B. Morphology Control Strategies for Solution-Processed Organic Semiconductor Thin Films. *Energy Environ. Sci.* **2014**, *7*, 2145–2159.
- (2) Patel, B. B.; Diao, Y. Multiscale Assembly of Solution-Processed Organic Electronics: The Critical Roles of Confinement, Fluid Flow, and Interfaces. *Nanotechnology* **2018**, *29*, No. 044004.
- (3) Duhm, S.; Heimel, G.; Salzmann, I.; Glowatzki, H.; Johnson, R. L.; Vollmer, A.; Rabe, J. P.; Koch, N. Orientation-Dependent Ionization Energies and Interface Dipoles in Ordered Molecular Assemblies. *Nat. Mater.* **2008**, *7*, 326–332.
- (4) Chen, W.; Huang, H.; Chen, S.; Huang, Y. L.; Gao, X. Y.; Wee, A. T. S. Molecular Orientation-Dependent Ionization Potential of Organic Thin Films. *Chem. Mater.* **2008**, *20*, 7017–7021.
- (5) Verlaak, S.; Beljonne, D.; Cheyns, D.; Rolin, C.; Linares, M.; Castet, F.; Cornil, J.; Heremans, P. Electronic Structure and Geminate Pair Energetics at Organic—Organic Interfaces: The Case of Pentacene/C60 Heterojunctions. *Adv. Funct. Mater.* **2009**, *19*, 3809—3814.
- (6) Xue, G.; Zhao, X.; Qu, G.; Xu, T.; Gumyusenge, A.; Zhang, Z.; Zhao, Y.; Diao, Y.; Li, H.; Mei, J. Symmetry Breaking in Side Chains Leading to Mixed Orientations and Improved Charge Transport in Isoindigo-Alt-Bithiophene Based Polymer Thin Films. ACS Appl. Mater. Interfaces 2017, 9, 25426–25433.
- (7) Liu, X.; He, B.; Garzón-Ruiz, A.; Navarro, A.; Chen, T. L.; Kolaczkowski, M. A.; Feng, S.; Zhang, L.; Anderson, C. A.; Chen, J.; Liu, Y. Unraveling the Main Chain and Side Chain Effects on Thin Film Morphology and Charge Transport in Quinoidal Conjugated Polymers. *Adv. Funct. Mater.* **2018**, *28*, No. 1801874.
- (8) Bai, X.; Zong, K.; Ly, J.; Mehta, J. S.; Hand, M.; Molnar, K.; Lee, S.; Kahr, B.; Mativetsky, J. M.; Briseno, A.; Lee, S. S. Orientation Control of Solution-Processed Organic Semiconductor Crystals to Improve out-of-Plane Charge Mobility. *Chem. Mater.* **2017**, 29, 7571–7578.
- (9) Oosterbaan, W. D.; Bolsée, J.-C.; Gadisa, A.; Vrindts, V.; Bertho, S.; D'Haen, J.; Cleij, T. J.; Lutsen, L.; McNeill, C. R.; Thomsen, L.; Manca, J. V.; Vanderzande, D. Alkyl-Chain-Length-Independent Hole Mobility Via Morphological Control with Poly(3-Alkylthiophene) Nanofibers. *Adv. Funct. Mater.* **2010**, *20*, 792–802.
- (10) Wu, K.-Y.; Hsieh, C.-T.; Wang, L.-H.; Hsu, C.-H.; Chang, S.-T.; Lan, S.-T.; Huang, Y.-F.; Chen, Y.-M.; Wang, C.-L. Influences of out-of-Plane Lattice Alignment on the Ofet Performance of Tips-Pen Crystal Arrays. *Cryst. Growth Des.* **2016**, *16*, 6160–6166.
- (11) Li, M.; An, C.; Marszalek, T.; Baumgarten, M.; Yan, H.; Mullen, K.; Pisula, W. Controlling the Surface Organization of Conjugated Donor-Acceptor Polymers by Their Aggregation in Solution. *Adv. Mater.* **2016**, *28*, 9430–9438.
- (12) Shen, Z.; Zhu, K.; O'Carroll, D. M. Aperiodic Porous Metasurface-Mediated Organic Semiconductor Fluorescence. *ACS Photonics* **2018**, *5*, 1215–1227.
- (13) Chae, S.; Cho, K. H.; Won, S.; Yi, A.; Choi, J.; Lee, H. H.; Kim, J.-H.; Kim, H. J. Favorable Face-on Orientation of a Conjugated Polymer on Roll-to-Roll-Transferred Graphene Interface. *Adv. Mater. Interfaces* **2017**, *4*, No. 1701099.
- (14) Hiszpanski, A. M.; Lee, S. S.; Wang, H.; Woll, A. R.; Nuckolls, C.; Loo, Y. L. Post-Deposition Processing Methods to Induce Preferential Orientation in Contorted Hexabenzocoronene Thin Films. ACS Nano 2013, 7, 294–300.
- (15) Chae, S.; Yi, A.; Lee, H. H.; Choi, J.; Kim, H. J. Laser-Induced Orientation Transformation of a Conjugated Polymer Thin Film with Enhanced Vertical Charge Transport. *J. Mater. Chem. C* **2018**, 6, 9374–9382.

- (16) Pan, G. X.; Chen, F.; Hu, L.; Zhang, K. J.; Dai, J. M.; Zhang, F. P. Effective Controlling of Film Texture and Carrier Transport of a High-Performance Polymeric Semiconductor by Magnetic Alignment. *Adv. Funct. Mater.* **2015**, 25, 5126–5133.
- (17) McCulloch, I.; Heeney, M.; Bailey, C.; Genevicius, K.; Macdonald, I.; Shkunov, M.; Sparrowe, D.; Tierney, S.; Wagner, R.; Zhang, W.; Chabinyc, M. L.; Kline, R. J.; McGehee, M. D.; Toney, M. F. Liquid-Crystalline Semiconducting Polymers with High Charge-Carrier Mobility. *Nat. Mater.* **2006**, *5*, 328–333.
- (18) Lee, M. J.; Gupta, D.; Zhao, N.; Heeney, M.; McCulloch, I.; Sirringhaus, H. Anisotropy of Charge Transport in a Uniaxially Aligned and Chain-Extended, High-Mobility, Conjugated Polymer Semiconductor. *Adv. Funct. Mater.* **2011**, *21*, 932–940.
- (19) Sirringhaus, H.; Wilson, R. J.; Friend, R. H.; Inbasekaran, M.; Wu, W.; Woo, E. P.; Grell, M.; Bradley, D. D. C. Mobility Enhancement in Conjugated Polymer Field-Effect Transistors through Chain Alignment in a Liquid-Crystalline Phase. *Appl. Phys. Lett.* **2000**, *77*, 406–408.
- (20) Bridges, C. R.; Ford, M. J.; Popere, B. C.; Bazan, G. C.; Segalman, R. A. Formation and Structure of Lyotropic Liquid Crystalline Mesophases in Donor–Acceptor Semiconducting Polymers. *Macromolecules* **2016**, 49, 7220–7229.
- (21) Bridges, C. R.; Ford, M. J.; Bazan, G. C.; Segalman, R. A. Molecular Considerations for Mesophase Interaction and Alignment of Lyotropic Liquid Crystalline Semiconducting Polymers. *ACS Macro Lett.* **2017**, *6*, 619–624.
- (22) Xie, R.; Aplan, M. P.; Caggiano, N. J.; Weisen, A. R.; Su, T.; Müller, C.; Segad, M.; Colby, R. H.; Gomez, E. D. Local Chain Alignment Via Nematic Ordering Reduces Chain Entanglement in Conjugated Polymers. *Macromolecules* **2018**, *51*, 10271–10284.
- (23) Trefz, D.; Gross, Y. M.; Dingler, C.; Tkachov, R.; Hamidi-Sakr, A.; Kiriy, A.; McNeill, C. R.; Brinkmann, M.; Ludwigs, S. Tuning Orientational Order of Highly Aggregating P(Ndi2od-T2) by Solvent Vapor Annealing and Blade Coating. *Macromolecules* **2019**, *52*, 43–54.
- (24) Bilger, D. W.; Figueroa, J. A.; Redeker, N. D.; Sarkar, A.; Stefik, M.; Zhang, S. Hydrogen-Bonding-Directed Ordered Assembly of Carboxylated Poly(3-Alkylthiophene)S. ACS Omega 2017, 2, 8526—8535
- (25) Zhang, S.; Pfefferle, L. D.; Osuji, C. O. Lyotropic Hexagonal Ordering in Aqueous Media by Conjugated Hairy-Rod Supramolecules. *Macromolecules* **2010**, 43, 7549–7555.
- (26) Park, M. S.; Aiyar, A.; Park, J. O.; Reichmanis, E.; Srinivasarao, M. Solvent Evaporation Induced Liquid Crystalline Phase in Poly(3-Hexylthiophene). *J. Am. Chem. Soc.* **2011**, *133*, 7244–7247.
- (27) Kleinhenz, N.; Rosu, C.; Chatterjee, S.; Chang, M.; Nayani, K.; Xue, Z.; Kim, E.; Middlebrooks, J.; Russo, P. S.; Park, J. O.; Srinivasarao, M.; Reichmanis, E. Liquid Crystalline Poly(3-Hexylthiophene) Solutions Revisited: Role of Time-Dependent Self-Assembly. *Chem. Mater.* **2015**, *27*, 2687–2694.
- (28) Kim, B. G.; Jeong, E. J.; Chung, J. W.; Seo, S.; Koo, B.; Kim, J. A Molecular Design Principle of Lyotropic Liquid-Crystalline Conjugated Polymers with Directed Alignment Capability for Plastic Electronics. *Nat. Mater.* **2013**, *12*, 659–664.
- (29) Yang, D. S.; Barlog, M.; Park, J.; Chung, K.; Shanker, A.; Sun, J.; Kang, J.; Lee, K.; Al-Hashimi, M.; Kim, J. Alignment of Lyotropic Liquid Crystalline Conjugated Polymers in Floating Films. *ACS Omega* **2018**, *3*, 14807–14813.
- (30) Park, K. S.; Kwok, J. J.; Dilmurat, R.; Qu, G.; Kafle, P.; Luo, X.; Jung, S.-H.; Olivier, Y.; Lee, J.-K.; Mei, J.; Beljonne, D.; Diao, Y. Tuning Conformation, Assembly, and Charge Transport Properties of Conjugated Polymers by Printing Flow. *Sci. Adv.* **2019**, *S*, No. eaaw7757.
- (31) Schott, S.; Gann, E.; Thomsen, L.; Jung, S. H.; Lee, J. K.; McNeill, C. R.; Sirringhaus, H. Charge-Transport Anisotropy in a Uniaxially Aligned Diketopyrrolopyrrole-Based Copolymer. *Adv. Mater.* **2015**, 27, 7356–7364.
- (32) Mohammadi, E.; Zhao, C.; Zhang, F.; Qu, G.; Jung, S.-H.; Zhao, Q.; Evans, C. M.; Lee, J.-K.; Shukla, D.; Diao, Y. Ion Gel

Dynamic Templates for Large Modulation of Morphology and Charge Transport Properties of Solution-Coated Conjugated Polymer Thin Films. ACS Appl. Mater. Interfaces 2019, 11, 22561–22574.

- (33) Qu, G.; Zhao, X.; Newbloom, G. M.; Zhang, F.; Mohammadi, E.; Strzalka, J. W.; Pozzo, L. D.; Mei, J.; Diao, Y. Understanding Interfacial Alignment in Solution Coated Conjugated Polymer Thin Films. ACS Appl. Mater. Interfaces 2017, 9, 27863–27874.
- (34) Mohammadi, E.; Zhao, C.; Meng, Y.; Qu, G.; Zhang, F.; Zhao, X.; Mei, J.; Zuo, J.-M.; Shukla, D.; Diao, Y. Dynamic-Template-Directed Multiscale Assembly for Large-Area Coating of Highly-Aligned Conjugated Polymer Thin Films. *Nat. Commun.* **2017**, 8, No. 16070.
- (35) Le Berre, M.; Chen, Y.; Baigl, D. From Convective Assembly to Landau-Levich Deposition of Multilayered Phospholipid Films of Controlled Thickness. *Langmuir* **2009**, *25*, 2554–2557.
- (36) Qu, G.; Kwok, J. J.; Mohammadi, E.; Zhang, F.; Diao, Y. Understanding Film-to-Stripe Transition of Conjugated Polymers Driven by Meniscus Instability. ACS Appl. Mater. Interfaces 2018, 10, 40692–40701.
- (37) Schuettfort, T.; Thomsen, L.; McNeill, C. R. Observation of a Distinct Surface Molecular Orientation in Films of a High Mobility Conjugated Polymer. *J. Am. Chem. Soc.* **2013**, *135*, 1092–1101.
- (38) Feidenhans'l, R. Surface Structure Determination by X-Ray Diffraction. Surf. Sci. Rep. 1989, 10, 105–188.
- (39) Sauer, T.; Arndt, T.; Batchelder, D. N.; Kalachev, A. A.; Wegner, G. The Structure of Langmuir—Blodgett Films from Substituted Phthalocyaninato-Polysiloxanes. *Thin Solid Films* **1990**, 187, 357—374.
- (40) O'Connor, B.; Kline, R. J.; Conrad, B. R.; Richter, L. J.; Gundlach, D.; Toney, M. F.; DeLongchamp, D. M. Anisotropic Structure and Charge Transport in Highly Strain-Aligned Regioregular Poly(3-Hexylthiophene). *Adv. Funct. Mater.* **2011**, *21*, 3697–3705
- (41) Patel, S. N.; Su, G. M.; Luo, C.; Wang, M.; Perez, L. A.; Fischer, D. A.; Prendergast, D.; Bazan, G. C.; Heeger, A. J.; Chabinyc, M. L.; Kramer, E. J. Nexafs Spectroscopy Reveals the Molecular Orientation in Blade-Coated Pyridal [2,1,3] Thiadiazole-Containing Conjugated Polymer Thin Films. *Macromolecules* 2015, 48, 6606–6616.
- (42) Gann, E.; Caironi, M.; Noh, Y.-Y.; Kim, Y.-H.; McNeill, C. R. Diffractive X-Ray Waveguiding Reveals Orthogonal Crystalline Stratification in Conjugated Polymer Thin Films. *Macromolecules* **2018**, *51*, 2979–2987.
- (43) Smilgies, D.-M.; Li, R.; Giri, G.; Chou, K. W.; Diao, Y.; Bao, Z.; Amassian, A. Look Fast: Crystallization of Conjugated Molecules During Solution Shearing Probed in-Situ and in Real Time by X-Ray Scattering. *Phys. Status Solidi RRL* **2013**, *7*, 177–179.
- (44) Yoneda, Y. Anomalous Surface Reflection of X Rays. *Phys. Rev.* **1963**, *131*, 2010–2013.
- (45) Furumi, S.; Ichimura, K. Surface-Assisted Photoalignment of Discotic Liquid Crystals by Nonpolarized Light Irradiation of Photo-Cross-Linkable Polymer Thin Films. *J. Phys. Chem. B* **2007**, *111*, 1277–1287.
- (46) Oosterbaan, W. D.; Bolsée, J.-C.; Wang, L.; Vrindts, V.; Lutsen, L. J.; Lemaur, V.; Beljonne, D.; McNeill, C. R.; Thomsen, L.; Manca, J. V.; Vanderzande, D. J. M. On the Relation between Morphology and Fet Mobility of Poly(3-Alkylthiophene)S at the Polymer/Sio2and Polymer/Air Interface. *Adv. Funct. Mater.* **2014**, *24*, 1994–2004.
- (47) Gruber, M.; Jung, S.-H.; Schott, S.; Venkateshvaran, D.; Kronemeijer, A. J.; Andreasen, J. W.; McNeill, C. R.; Wong, W. W. H.; Shahid, M.; Heeney, M.; Lee, J.-K.; Sirringhaus, H. Enabling High-Mobility, Ambipolar Charge-Transport in a Dpp-Benzotriazole Copolymer by Side-Chain Engineering. *Chem. Sci.* **2015**, *6*, 6949–6960.
- (48) Jiang, Z. Gixsgui: A Matlab Toolbox for Grazing-Incidence X-Ray Scattering Data Visualization and Reduction, and Indexing of Buried Three-Dimensional Periodic Nanostructured Films. *J. Appl. Crystallogr.* **2015**, *48*, 917–926.

- (49) Cowie, B. C. C.; Tadich, A.; Thomsen, L. The Current Performance of the Wide Range (90–2500 Ev) Soft X-Ray Beamline at the Australian Synchrotron. *AIP Conf. Proc.* **2010**, 1234, 307–310.
- (50) Gann, E.; McNeill, C. R.; Tadich, A.; Cowie, B. C. C.; Thomsen, L. Quick as Nexafs Tool (Qant): A Program for Nexafs Loading and Analysis Developed at the Australian Synchrotron. *J. Synchrotron Radiat.* **2016**, 23, 374–380.
- (51) Nahid, M. M.; Gann, E.; Thomsen, L.; McNeill, C. R. Nexafs Spectroscopy of Conjugated Polymers. *Eur. Polym. J.* **2016**, *81*, 532–554.
- (52) White, J. L.; Spruiell, J. E. The Specification of Orientation and Its Development in Polymer Processing. *Polym. Eng. Sci.* **1983**, 23, 247–256.
- (53) Tao, Y.; Zohar, H.; Olsen, B. D.; Segalman, R. A. Hierarchical Nanostructure Control in Rod-Coil Block Copolymers with Magnetic Fields. *Nano Lett.* **2007**, *7*, 2742–2746.

NOTE ADDED AFTER ASAP PUBLICATION

This paper was published ASAP on July 8, 2020, with incorrect graphics for Figures 5 and 6. The corrected version was reposted on July 9, 2020.